

Optical appearance of a boson star with soliton potential

Ke-Jian He,^{a*} Guo-Ping Li,^{b†} Chen-Yu Yang,^{a‡} Xiao-Xiong Zeng^{a,c§}

^a*Department of Mechanics, Chongqing Jiaotong University, Chongqing 400000, People's Republic of China*

^b*School of Physics and Astronomy, China West Normal University, Nanchong 637000, People's Republic of China*

^c*College of Physics and Electronic Engineering, Chongqing Normal University, Chongqing 401331, People's Republic of China*

Abstract

In this paper, we conduct an in-depth investigation into the optical images of boson stars with the solitonic potential. In the context of a celestial source and a thin accretion disk, the optical characteristics of the soliton boson star have been derived. Considering the influence of the initial scalar field ψ_0 and a larger coupling parameter α (the weak coupling case), the optical images of boson stars primarily exhibit direct and lensed images. The results demonstrate that variations in ψ_0 and α influence the image size, whereas the observer's inclination angle θ has a substantial impact on the image shape. In contrast, when the coupling parameter α is small (the strong coupling case), a sub-annular structure emerges within the Einstein ring for a spherically symmetric light source. In the presence of a thin accretion disk, higher-order gravitational lensing images emerge, indicating that photons are capable of orbiting the equatorial plane of the boson star multiple times. We also analyze how the effective potential and redshift factor depend on the parameters ψ_0 , α , and θ . The results indicate that at smaller values of θ , gravitational redshift is the dominant effect, resulting in an optical image featuring a bright ring surrounding a comparatively dim central region. At larger values of θ , the Doppler effect becomes more pronounced, resulting in a substantial brightness disparity between the left and right sides of the optical image. These findings offer robust theoretical underpinnings for differentiating solitonic boson stars from black holes via high-resolution astronomical observations.

*E-mail: kjhe94@163.com

†E-mail: gpliphys@yeah.net

‡E-mail: chenyuyang2024@163.com

§E-mail: xxzengphysics@163.com (Corresponding author)

1 Introduction

Since the formulation of general relativity (GR) [1], this theory has played a fundamental role in modern physics. In 1919, the observation of the gravitational deflection of light by the Sun confirmed the validity of GR [2], marking the beginning of a new era in gravitational physics. A century later, in 2019, the Event Horizon Telescope (EHT) successfully captured the first direct image of a black hole's shadow [3]. When a sufficiently compact object is illuminated by its own accretion disk, a prominent bright ring is formed, which is accompanied by a central region of reduced brightness. Owing to the intense gravitational influence exerted by the compact object, the trajectory of light is significantly deflected in the vicinity of the object, a phenomenon known as gravitational lensing [4]. These bright rings are composed of photons that have undergone strong gravitational lensing [5, 6]. In fact, the optical image produced by the superheated plasma surrounding the supermassive object at the center of the M87 galaxy is in full agreement with this theoretical prediction. In 2022, the EHT released an image of the shadow of the Sagittarius A* (Sgr A*) black hole at the center of the Milky Way, which similarly exhibited a bright ring [7]. These findings not only corroborate the accuracy and validity of GR in the regime of strong gravitational fields, but also offer a valuable opportunity to examine the properties of ultra-compact objects from both theoretical and observational perspectives. [8].

There is no doubt that the critical curve plays a crucial role in the study of optical images of ultra-compact objects. For instance, within the spacetime of a Kerr black hole, there exists a photon shell situated at an unstable orbit. This corresponds to the critical point of the radial "potential," where light rays asymptotically approach but do not cross [9, 10]. In the absence of spin, the photon shell degenerates into a single circular critical curve corresponding to the extremum of the effective potential, which is referred to as the photon sphere. A substantial body of research has investigated this theoretical framework and its potential empirical implications [11–13]. Research has demonstrated that for any compact object situated within its photon sphere, light rays are capable of orbiting multiple times, thereby forming a distinct photon ring embedded within the primary bright ring of emitted radiation. These photon rings vanish at the outer edge of the central brightness depression, i.e., the shadow. The dimensions and intensity of the shadow, along with the positioning and luminosity of the photon rings, are dictated by the synergistic influence of the background spacetime geometry, optical attributes, and radiative properties of the accretion disk surrounding the object. [14]. Separating the contributions of the background geometry and the astrophysical properties of the disk in shadow images remains a critical challenge [15, 16], and whether the Kerr solution can effectively describe every compact object remains a subject of debate [17].

The shadow images of black holes under different accretion disk models have been extensively studied [18–38]. In addition, some important results have been obtained on black hole shadows and photon rings using wave optics in the holographic framework [39–44]. However, beyond black holes, many other compact objects with distinct physical properties are theoretically expected to exist in the universe, as discussed in [45, 46]. In terms of optical images (or shadows), these objects may exhibit differences in the structure of their photon spheres, such as possessing multiple photon rings or

lacking photon rings entirely [47–51], providing a theoretical basis for distinguishing various compact objects through optical images. For instance, it has been demonstrated that for asymptotically flat exotic compact objects without an event horizon, an even number of photon rings must exist if their spacetime is topologically trivial [52]. This study focuses on boson stars, which are ultra-compact objects composed of bosons bound by self-gravity, with their mass and size ranging from atomic to astrophysical scales, depending on the boson mass. Since the pioneering work of Kaup [53] and Ruffini and Bonnazol [54], boson stars have attracted significant attention, and their stability and dynamical properties have been extensively studied [55,56]. It is now widely accepted that, by selecting appropriate model parameters, numerical simulations can produce rotating or non-rotating boson stars with several solar masses, which are consistent with astronomical observations but lack an event horizon. Based on this, it has been proposed that the supermassive object at the center of the Milky Way, Sgr A*, could be a boson star [57]. Boson stars and their optical images under different potentials and gravitational modifications have been studied [58–60], including mini boson stars [61]. Due to the similarity between black hole shadows and boson star optical images, some studies have suggested that boson stars can mimic the shadow of a Schwarzschild black hole under a truncated accretion disk [62] and at smaller observer inclination angles [63], making boson stars a viable alternative to black hole models.

One significant distinction between boson stars and black holes lies in the incorporation of a self-interaction potential [64]. This feature facilitates the formation of bound states even in the absence of gravitational forces, a phenomenon referred to as Q-balls [65]. In a shift-symmetric theory, the self-interaction potential is typically composed of a quadratic, a quartic, and a sextic term, such as $V = c_2\psi^2 + c_4\psi^4 + c_6\psi^6$, where $c_2, c_6 > 0, c_4 < 0$. This study focuses on an interesting special case of the sextic potential, commonly referred to as the solitonic potential, which takes the form $V = u^2\psi^2(1 - \frac{\psi^2}{\alpha^2})^2$ [66], where the interaction term is governed by the parameter α . A characteristic feature of this theory is that in the false vacuum, the potential satisfies $V = 0$ at $\psi = \alpha$. When α is large, the system resembles a mini boson star; however, as α decreases, the equations of motion exhibit greater stiffness, making them increasingly difficult to solve. This study aims to investigate the optical images of solitonic boson stars under spherical light sources and thin accretion disks using numerical methods. We successively consider the effects of the initial scalar field ψ_0 , weak coupling, and strong coupling, corresponding to larger and smaller coupling parameters α , respectively. In the first two cases, due to the absence of a critical curve, solitonic boson stars lack the photon ring structure of a Kerr black hole. Their optical images are primarily dominated by the direct image of the accretion disk, forming a single bright ring with a central brightness depression. However, under strong coupling, the optical images of solitonic boson stars resemble black hole shadows.

The structure of this paper is as follows: Section 2 derives the equations of motion based on the solitonic potential. Section 3 describes the numerical methods for spherical light sources, while Section 4 presents those for thin accretion disks. Section 5 presents the numerical results and provides a detailed discussion of the optical images and redshift factors of solitonic boson stars under different conditions. Finally, Section 6 concludes with a summary and discussion.

2 Solutions of solitonic boson stars

Considering the following action of minimal coupling of a complex scalar field with a gravitational field

$$S = \int d^4x \sqrt{-g} \left[\frac{R}{2\kappa} - \nabla_b \bar{\Psi} \nabla^b \Psi - V(|\Psi|^2) \right], \quad (1)$$

where g is the determinant of the metric, R is the curvature scalar, $\kappa = 8\pi$ is the coupling constant, $\bar{\Psi}$ is the complex conjugate of the scalar field Ψ , and V is the scalar potential. In this paper, we are interested in a solitonic potential

$$V(|\Psi|^2) = u^2 \psi^2 \left(1 - \frac{\psi^2}{\alpha^2} \right)^2, \quad (2)$$

in which u is the scalar field mass and α is a free parameter controlling the self-interaction. The self-interaction potential here is a standard choice so that it can provide configurations which can exist even in flat spacetime [67]. Variation of the corresponding action with respect to the metric and field gives the equations of motion

$$R_{bc} - \frac{1}{2} R g_{bc} = \kappa T_{bc}, \quad (3)$$

$$g^{bc} \nabla_b \nabla_c \Psi = \Psi \frac{dV}{d|\Psi|^2}, \quad (4)$$

with energy-momentum tensor

$$T_{bc} = \nabla_b \bar{\Psi} \nabla_c \Psi + \nabla_c \bar{\Psi} \nabla_b \Psi - g_{bc} (\nabla_d \bar{\Psi} \nabla^d \Psi + V). \quad (5)$$

Supposing the solution as the the general, spherical symmetric metric in Schwarzschild-like coordinates

$$ds^2 = -f(r) dt^2 + g(r)^{-1} dr^2 + r^2 (d\theta^2 + \sin^2 \theta d\phi^2), \quad (6)$$

with

$$\Psi(r, t) = \psi(r) e^{i\omega t}. \quad (7)$$

Substituting Eq.(2), Eq.(6) and Eq.(7) into Eq.(3) and Eq.(4), we can get the following equations of motion

$$\frac{df}{dr} = \frac{f(1-g)}{gr} + \kappa r \left(\frac{\omega^2 \psi^2}{g} + f \left(\frac{d\psi}{dr} \right)^2 - \frac{f}{g} u^2 \psi^2 \left(1 - \frac{\psi^2}{\alpha^2} \right)^2 \right), \quad (8)$$

$$\frac{dg}{dr} = \frac{1-g}{r} - g\kappa r \frac{d\psi^2}{dr} - \frac{\kappa r \left(f \mu^2 \psi^2 \left(1 - \frac{\psi^2}{\alpha^2} \right)^2 + \psi^2 \omega^2 \right)}{f}, \quad (9)$$

$$\frac{d^2\psi}{dr^2} = -\frac{1}{2} \left(\frac{df}{f} + \frac{dg}{g} + \frac{4}{r} \right) \frac{d\psi}{dr} - \frac{\psi \left(\mu^2 \left(-\frac{3\psi^4}{\alpha^4} + \frac{4\psi^2}{\alpha^2} - 1 \right) + \frac{\omega^2}{f} \right)}{g}. \quad (10)$$

The above equations of motion are invariant under the following scale change

$$r \rightarrow ur, \quad f \rightarrow u^2 f, \quad g \rightarrow r, \quad V \rightarrow u^{-2} V. \quad (11)$$

So without losing generality, we will set $u = 1$ later. It is very difficult to solve the above equations of motion directly, usually we need to solve it by numerical method, in this case we need to find the boundary conditions of $f(r)$, $g(r)$ and $\psi(r)$. At infinity, we hope its asymptotic behavior similar is to the Schwarzschild space time, that is

$$f(r \rightarrow \infty) \sim f_\infty \left(1 - \frac{2M}{r}\right), \quad (12)$$

$$g(r \rightarrow \infty) \sim \left(1 - \frac{2M}{r}\right), \quad (13)$$

$$\psi(r \rightarrow \infty) \sim 0. \quad (14)$$

Since we are interested in localized solutions of the scalar field Ψ that preserve asymptotic flatness, the wave function ψ thus decay exponentially as $r \rightarrow \infty$. On the other hand, at $r = 0$, the solutions should be convergent. After expand $f(r)$, $g(r)$, $\psi(r)$ into a power series of r at $r = 0$, we will get

$$f(r \rightarrow 0) \sim f_0, \quad g(r \rightarrow 0) \sim 1, \quad \psi(r \rightarrow 0) \sim \psi_0. \quad (15)$$

In fact, f_∞ and f_0 are not independent, as f_∞ is given, f_0 will be determined. Since the equations of motion are independent of the time t , we can reparameterize t , f and ω with any constant. That is, with the transformation

$$t \rightarrow at, \quad f \rightarrow a^{-2}f, \quad \omega \rightarrow a^{-1}\omega, \quad (16)$$

the system will not change. In this case, we can set $f_0 = 1$. Since boson stars are similar to the ideal fluid stars, we can also characterize the solution in terms of their total mass M and radius R . Both of these quantities can be defined by the following mass function

$$m(r) = \frac{r}{2}(1 - g(r)) \quad (17)$$

The ADM mass is defined as $M = m(r \rightarrow \infty)$, and the radius of the star is set at $R = 0.98M$. With the boundary conditions mentioned above, we can solve the equations of motion with fixed values of α and ψ_0 .

3 Shadow images with spherical light sources

In this section, we will discuss the shadow images of boson stars illuminated by a spherical light source. We will discuss it in terms of ray tracing, for which it is very important to determine the motion of photons around the boson stars, which satisfy the following Euler-Lagrangian equation

$$\frac{d}{d\gamma} \left(\frac{\partial \mathcal{L}}{\partial \dot{x}^\alpha} \right) = \frac{\partial \mathcal{L}}{\partial x^\alpha} \quad (18)$$

in which γ is the affine parameter, \dot{x}^α is the four-velocity of the photon and \mathcal{L} is the Lagrangian, which can be written as

$$\begin{aligned} 0 = \mathcal{L} &= -\frac{1}{2} g_{\alpha\beta} \dot{x}^\alpha \dot{x}^\beta \\ &= -\frac{1}{2} (-f(r) \dot{t}^2 + \frac{1}{g(r)} \dot{r}^2 + r^2 (\dot{\theta}^2 + \sin^2 \theta \dot{\phi}^2)) \end{aligned} \quad (19)$$

The metric function does not explicitly contain time t and the azimuthal angle ϕ , thus two conserved quantities exist

$$E = \frac{\partial \mathcal{L}}{\partial \dot{t}} = f(r) \frac{dt}{d\gamma} \quad (20)$$

$$L = -\frac{\partial \mathcal{L}}{\partial \dot{\phi}} = r^2 \frac{d\phi}{d\gamma} \quad (21)$$

With Eq.(19), Eq.(20) and Eq.(3), we can obtain the four-velocity components for time, azimuthal angle, and radial direction, which are

$$\frac{dt}{d\gamma} = \frac{1}{bf(r)} \quad (22)$$

$$\frac{d\phi}{d\gamma} = \pm \frac{1}{r^2} \quad (23)$$

$$\frac{dr}{d\gamma} = \sqrt{\frac{1}{b^2} \frac{g(r)}{f(r)} - \frac{1}{r^2} g(r)} \quad (24)$$

Here, "+" represents the clockwise direction and "-" represents the counterclockwise direction. The impact parameter b is defined as

$$b = \frac{|L|}{E} \quad (25)$$

The effective potential in this case can be defined as

$$V_{eff} \equiv -\frac{1}{2} \dot{r}^2 + C = -\frac{1}{2} \left[\frac{1}{b^2} \frac{g(r)}{f(r)} - \frac{1}{r^2} g(r) \right] + \frac{1}{2b^2}. \quad (26)$$

If there is photon sphere, the motion of the photon satisfies $\dot{r} = 0$, $\ddot{r} = 0$, which result in from Eq.(26)

$$V_{eff}(r_{ph}) = \frac{1}{2b_{ph}^2}, \quad V_{eff}(r_{ph})' = 0. \quad (27)$$

where $b_{ph} = b(r_{ph})$ is the critical impact parameter, r_{ph} is the radius of the photon sphere, and V'_{eff} is the derivative with respect to r .

To determine the motion of the photon, it is not enough to just have the geodesic equation, we also need to give the initial conditions of evolution, and for that we need to choose one observer in the spacetime. We assume that a zero-angular-momentum observer (ZAMO) observer is located at coordinates $(t_o, r_o, \theta_o, \phi_o)$. A locally orthogonal normalized frame may exist in the neighborhood of the observer, which are

$$\hat{e}_0 = \frac{1}{\sqrt{-g_{tt}}} \partial_t, \quad \hat{e}_1 = -\frac{1}{\sqrt{g_{rr}}} \partial_r, \quad \hat{e}_2 = \frac{1}{\sqrt{g_{\theta\theta}}} \partial_\theta, \quad \hat{e}_3 = -\frac{1}{\sqrt{g_{\phi\phi}}} \partial_\phi, \quad (28)$$

In the observer's frame, the tangent vector of the null geodesic can be written as

$$\dot{s}_o = |\overrightarrow{OP}| (-\hat{e}_0 + \cos \Theta \hat{e}_1 + \sin \Theta \cos \Xi \hat{e}_2 + \sin \Theta \sin \Xi \hat{e}_3), \quad (29)$$

in which $|\overrightarrow{OP}|$ represents the tangent vector of the null geodesic at the point O in the three-dimensional subspace, and Θ denotes the angle between $|\overrightarrow{OP}|$ and \hat{e}_1 , Ξ denotes the angle between $|\overrightarrow{OP}|$ and \hat{e}_2 . The celestial coordinates are the coordinates described by (Θ, Ξ) .

On the other hand, for each light ray $s(\alpha)$ with coordinate representation $t(\alpha)$, $r(\alpha)$, $\theta(\alpha)$ and $\phi(\alpha)$, the general form of tangent vector is

$$\dot{s} = \dot{t}\partial_t + \dot{r}\partial_r + \dot{\theta}\partial_\theta + \dot{\phi}\partial_\phi, \quad (30)$$

By comparing Eq.(29) and Eq.(30), we conclude that once the value of the four-momentum of a photon is given, the celestial coordinates are determined. Vice versa, If the celestial coordinates are known, then four-momenta can be obtained by coordinate transformation. So, combined with the position of the observer, the initial value of the photon motion equation can be obtained directly.

In order to obtain the image of the black hole, it is finally necessary to correspond the celestial coordinate (Θ, Ξ) to the point (x, y) on the imaging plane one by one. The image plane is divided into n equal squares, and at any position with pixel coordinate (i, j) , the celestial coordinates can be expressed as

$$\tan \Xi = \frac{2j - (n + 1)}{2i - (n + 1)} \quad (31)$$

$$\tan \Psi = \frac{1}{n} \tan \frac{1}{2} \beta_{\beta_{\text{fov}}} \sqrt{\left(i - \frac{n+1}{2}\right)^2 + \left(j - \frac{n+1}{2}\right)^2} \quad (32)$$

in which $\beta_{\beta_{\text{fov}}}$ is the angle of field of view. When the pixels and the angle of field of view are determined, the celestial coordinates and the initial conditions are determined, further we can calculate the motion of the photon in the spacetime of the boson star based on the motion equation of the photon.

4 Shadow images with thin accretion disks

In this section, we intend to investigate the shadow images of boson stars illuminated by the accretion disk, which is assumed to be located on the equatorial plane and be thin both geometrically and optically. The light source is connected with the ZAMO oberver by the light ray. Usually, when the light ray interacts with the thin accretion disk, the intensity would change due to the emission and absorption. As in [68], we ignore the refraction effect, the change of the intensity in this case is

$$\frac{d}{d\gamma} \left(\frac{Q_\nu}{\nu^3} \right) = \frac{J_\nu - k_\nu Q_\nu}{\nu^2} \quad (33)$$

in which γ is the affine parameter of null geodesics as mentioned above, Q_ν , J_ν , and k_ν are the specific intensity, emissivity and absorption coefficient at the frequency ν respectively. When the light propagates in vacuum, J_ν and k_ν vanish, $\frac{Q_\nu}{\nu^3}$ thus is conserved along the geodesics.

In the thin disk approximation, only the instantaneous emission and absorption on the equatorial plane should be considered, that is, J_ν and k_ν vanish except on the equatorial plane. In this case, we can write the total light intensity observed by the observer as

$$Q_0 = \sum_n^{n_{\text{max}}} f_n \left(\frac{\nu_0}{\nu_n} \right)^3 J_n \quad (34)$$

where n is the number of times that the light passes through the equatorial plane, f_n is the absorption of the accretion disk, J_n is the emission of the accretion disk, and $\frac{\nu_0}{\nu_n} \equiv g_n$ is the redshift factor.

To determine the intensity Q_0 , we should find f_n , J_n and g_n firstly. As stressed in [34], because f_n mainly changes the strength of the narrow photon ring, it has limited effect on overall image, so we set it to 1. There are many choices of J_n , for the black hole, to compare with astronomical observations, such as images of M87 and Sgr A*, the emissivity is often regarded as a second-order polynomial in log-space. Here we choose the Gralla-Lupsasca-Marrone model [21]

$$J = \frac{\exp\left(-\frac{1}{2}\left(\epsilon + \sinh^{-1}\left(\frac{r-\zeta}{\eta}\right)\right)^2\right)}{\sqrt{(r-\zeta)^2 + \eta^2}} \quad (35)$$

This model is also prevailing for its predictions agree with those of general relativistic magnetohydrodynamics simulations of astrophysical accretion disks [14]. In Eq.(4), the term of ϵ , ζ and η are parameters controlling the shape of the emission profile, which are called as the rate of increase, radial translation, and the dilation of the profile, respectively. In principle, we can adjust these parameters to select proper intensity profiles for the models under study. In this paper, we consider $\epsilon = 0$, $\zeta = 6M$, and $\eta = M$. The other quantity we need to calculate is the redshift factor g_n . In our model, the accretion flow is electrically neutral plasma, which moves along timelike geodesics with conserved quantities E , L , and angular velocity

$$\Omega_n = \frac{u^\phi}{u^t} \Big|_{r=r_n} \quad (36)$$

where $n = 1 \dots N_{max}$ is the number of times that the ray crosses the equatorial plane, and we use the subscript n to denote the corresponding measurements in the local rest frame. In this case the redshift factor can be written as

$$g_n = -\frac{1}{\Sigma(1 - b\Omega_n)} \quad (37)$$

in which we have defined

$$\Sigma = \sqrt{\frac{1}{g_{tt} + g_{\phi\phi}\Omega_n^2}} \Big|_{r=r_n} \quad (38)$$

With this equation, we will discuss only the light intensity by substituting it into Eq.(33), but also the redshift.

5 Numeric results

After providing the above theory, we will obtain the solution of the boson stars by numerical method and study their shadows under different light sources. In principle, the solution of the boson star depends on the initial scalar field ψ_0 and the coupling parameter α . We first study the effect of the initial wave function on the configurations and shadows of the boson stars with fixed coupling parameters, i.e. the case of variable scalar field. Then we will fix the initial scalar field to study the effects of coupling parameters on the configurations and shadows of the boson stars. At this point,

we will consider the case of weak coupling and strong coupling, that is, the case of large and small coupling constant relatively.

5.1 Variable scalar field

In this section, we will set $\alpha = 0.9$ and investigate the effect of scalar field ψ_0 on the configurations and shadows of the boson stars. Firstly, we will obtain the numerical solutions of the scalar field and the metric, and then get the fitting function of the metric through fitting method. Finally, the shadows of the boson stars will be investigated respectively under spherically light source and thin disk accretion by fitting metric.

The numeric results for different scalar field ψ_0 is shown in Figure 1. We can see that the scalar field exist only in a narrow range and it decline rapidly to zero as r increases for all the boson star models. The metric of the boson stars are shown in Figure 2. For comparison with the simplest spherically symmetric black holes, we also draw the metric of Schwarzschild black hole. From the left subfigure, we find that, as expected, boson stars have no horizon since the metrics do not vanishes, which is different from the Schwarzschild black hole. But the asymptotic behavior of boson stars are exactly the same as that of Schwarzschild black hole. That is, as r increases, the metrics approach to one. In particular, when r is around $10M$, boson stars are exactly the same as the Schwarzschild black holes. The right subfigure in Figure 2 is the g_{rr} components of bosons stras and Schwarzschild black hole. We find they are not divergent for they have no horizons. Interestingly, the metric components g_{rr} converge to the same value for different initial conditions ψ_0 .

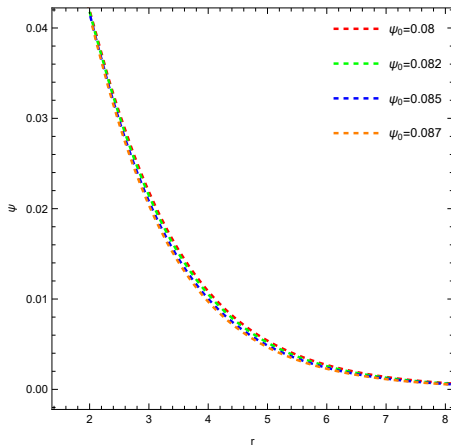


Figure 1: Variation of the scalar field ψ as a function of the radial distance r for different initial scalar field values ψ_0 , with the coupling parameter $\alpha = 0.9$.

After obtaining the solutions of boson stars, we can study their shadows by numerical method in principle. But to make it easier, we will assume some specific functions to fit the metric components. It was found that the following functions can fit perfectly

$$g_{tt} = -\exp \left[p_7 \left(\exp \left(-\frac{1 + p_1 r + p_2 r^2}{p_3 + p_4 r + p_5 r^2 + p_6 r^3} \right) - 1 \right) \right], \quad (39)$$

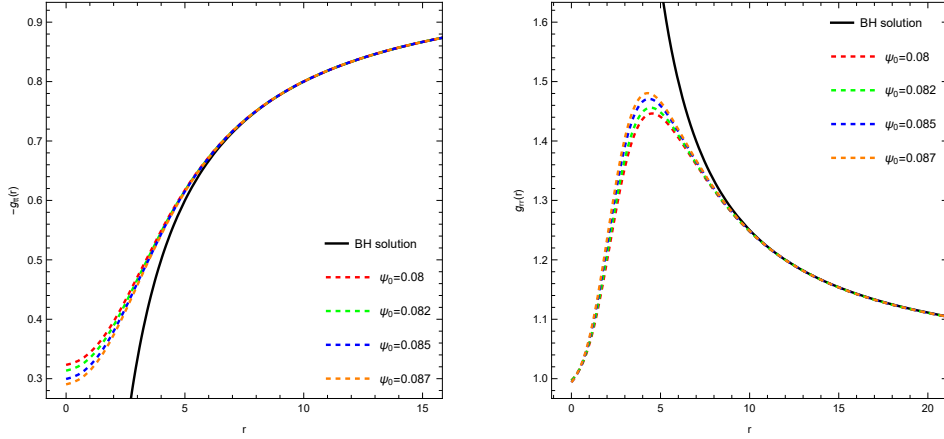


Figure 2: Comparison between the numerical metrics and the Schwarzschild black hole metric components for different initial scalar field values ψ_0 , with the coupling parameter $\alpha = 0.9$. The mass of the Schwarzschild BH is 1.

$$g_{rr} = \exp \left[q_7 \left(\exp \left(-\frac{1 + q_1 r + q_2 r^2}{q_3 + q_4 r + q_5 r^2 + q_6 r^3} \right) - 1 \right) \right]. \quad (40)$$

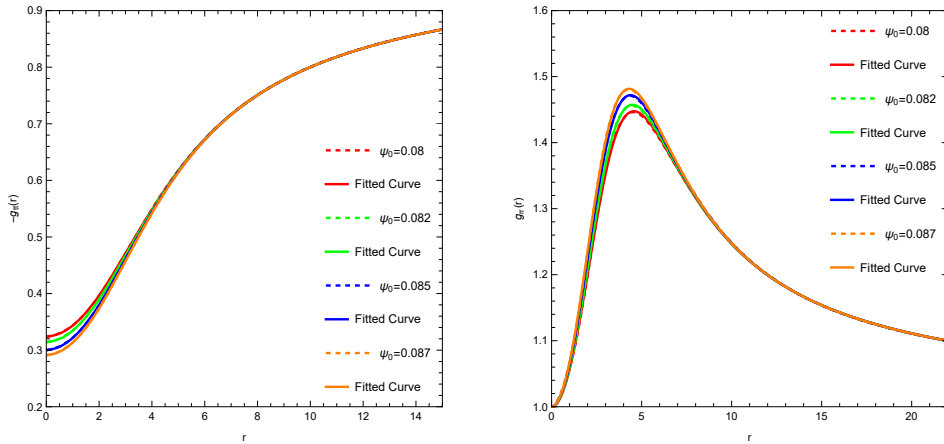


Figure 3: Comparison between the numerical metrics and the fitting functions for different initial scalar field values ψ_0 , with the coupling parameter $\alpha = 0.9$. The dashed lines represent the numerical metrics, while the solid lines represent the fitting functions.

The fitting results are shown in Figure 3. The numerical results are represented by dotted lines and the fitting results by solid lines. It is not difficult to find that, for both the g_{tt} and g_{rr} , the numerical results and the fitting results exactly coincide. Table 1 and Table 2 give the parameter values of the fitting functions of the metric components respectively. Meanwhile, we also give the mass of the boson star, which decreases as the initial value of ψ_0 increases.

Table 1. Parameter estimates of $p_i (i = 1, \dots, 7)$ in the fitting function (39) for the metric component g_{tt} , with the coupling parameter $\alpha = 0.9$. $m(r)$ represents the mass of the boson star.

Type	ψ_0	$m(r)$	p_1	p_2	p_3	p_4	p_5	p_6	p_7
SBS1	0.08	0.603	0.024	0.113	-0.367	-0.013	-0.051	-0.007	-0.079
SBS2	0.082	0.6	0.026	0.119	-0.367	-0.014	-0.054	-0.008	-0.082
SBS3	0.085	0.595	0.027	0.127	-0.365	-0.014	-0.057	-0.009	-0.083
SBS4	0.087	0.591	0.029	0.134	-0.365	-0.015	-0.06	-0.01	-0.086

Table 2. Parameter estimates of $q_i (i = 1, \dots, 7)$ in the fitting function (40) for the metric component g_{rr} , with the coupling parameter $\alpha = 0.9$. $m(r)$ represents the mass of the boson star.

Type	ψ_0	$m(r)$	q_1	q_2	q_3	q_4	q_5	q_6	q_7
SBS1	0.08	0.603	-17.515	-2.315	6.652	1.03	1.545	0.032	0.02
SBS2	0.082	0.6	-16.16	-2.199	6.127	0.935	1.486	0.033	0.022
SBS3	0.085	0.595	-10.702	-1.356	4.323	0.553	1.075	0.026	0.029
SBS4	0.087	0.591	-10.945	-1.454	4.333	0.572	1.132	0.029	0.029

We can also plot the effective potential of the boson stars via Eq.(26). We find that there are not convex barriers outside the boson stars as the Schwarzschild black holes. In other words, for SBS1-SBS4, there are not photon rings.

The relationship between the effective potential and the radius is shown in Figure 4 . We can see that, as the Schwarzschild black hole, there are always potential barriers. For large boson stars, the potential barrier is more prominent. When a photon travels from infinity to the boson star, it will be scattered back if it encounters a barrier. When the photon does not encounter the barrier, the photon will fall into the boson star. And when the photon reaches the top of the barrier, the photon will move in a circle around the boson star, and the corresponding trajectory is the photon sphere.

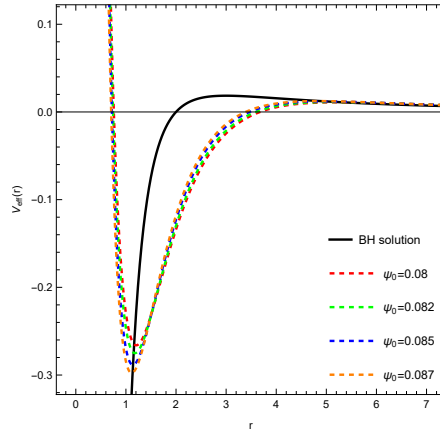


Figure 4: Variation of the effective potential $V_{eff}(r)$ as a function of the radial distance r for boson stars and the Schwarzschild black hole for different initial scalar field values ψ_0 , with the impact parameter $b = 1$ and the coupling parameter $\alpha = 0.9$. The dashed lines represent boson stars, while the solid lines represent the Schwarzschild black hole.

The shadows of different boson stars with spherical light source are shown in Figure 5. In each figure, the celestial sphere has been divided into four different quadrants marked with different colors.

The grid of both longitude and latitude lines are denoted with brown lines positioned by 10° . The black transparency region in the center is the shape of boson star. From these figures, we can see some interesting phenomena. Unlike black holes, light is not completely absorbed when it enters the star, but remains there. Like black holes, there is lensing effect in addition to direct radiation after the light source passes through the star. More importantly, Einstein rings still exist, which is denoted by white circle. We also study the effect of the observation angle and initial value ψ_0 on the shadow image. We find that the observation angle has very little effect on the image, but the effect on ψ_0 is very significant.

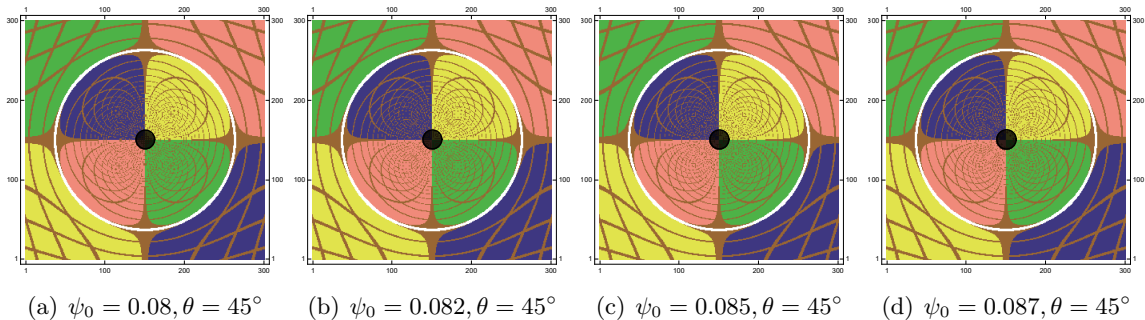


Figure 5: Optical images of boson stars illuminated by a spherical light source for different initial scalar field values ψ_0 , with the coupling parameter $\alpha = 0.9$, the angle of field of view $\beta_{\text{fov}} = 45^\circ$, and the observer located at $r_{\text{obs}} = 50m(r)$, where $m(r)$ represents the mass of the boson star. The black transparent region represents the boson star, while the white ring corresponds to the Einstein ring.

In Figure 6, we present the optical images of boson stars illuminated by a thin accretion disk as the light source. We fix the angle of field of view at $\beta_{\text{fov}} = 10^\circ$, the coupling parameter at $\alpha = 0.9$, and the observer distance at $r_{\text{bos}} = 200$. In the images, purple represents an intensity of $Q_0 = 0$, white corresponds to $(Q_0)_{\text{max}}$, and the color varies linearly with increasing intensity. All images exhibit a structure featuring a central region with zero intensity, surrounded by one or more bright rings. The dark central region corresponds to the boson star, while the bright rings are formed by light passing through the equatorial plane of the boson star one or multiple times. It can be observed that as the observer inclination approaches $\theta \rightarrow 0^\circ$ (the first column), the optical image of the boson star appears as a symmetric circular ring, corresponding to the direct image, with no lensed image present. The initial scalar field ψ_0 does not significantly affect the size and shape of the direct image. When θ increases to 30° (the second column), the direct image slightly deforms into an elliptical shape, with the left side exhibiting a greater intensity than the right. As ψ_0 increases to 0.087, a faint lensed image begins to appear. When θ increases to 60° (the third column), a noticeable lensed image emerges, and as ψ_0 increases, the direct image remains almost unchanged while the lensed image grows. In this case, both the direct and lensed images undergo significant deformation into a D-shaped structure. When θ further increases to 75° (the fourth column), the lensed image size increases significantly, and as ψ_0 continues to grow, the lensed image enlarges further. At this stage, the left side of the direct image exhibits greater intensity than the right, and the intersection point between the direct and lensed images on the left is also brighter than that on the right. Interestingly, at larger observer

inclinations (60° and 75° , i.e., the third and fourth columns), the optical images of boson stars exhibit lensed images, and the direct and lensed images intersect.

It is worth noting that when $\theta \rightarrow 0^\circ$, the direct image appears as a perfect circular ring, with no lensed image present. This is because the observer's line of sight is perpendicular to the equatorial plane and coincides with the symmetry axis of the accretion disk and the boson star. At this angle, the radial velocity of each point on the accretion disk relative to the observer is nearly zero, with only tangential velocity contributing, so the observed redshift is primarily due to gravitational redshift. As θ increases, the influence of radial velocity on the observer strengthens, leading to an increasing Doppler redshift. Further analysis reveals that when $\theta \neq 0$, light rays orbit the boson star. If the light rays travel toward the observer, the Doppler effect induces a blueshift, increasing the photon energy and making the optical image brighter; conversely, if the light rays move away from the observer, the Doppler effect causes a redshift, decreasing the photon energy and dimming the optical image. From the images corresponding to $\theta = 30^\circ, 60^\circ, 75^\circ$ (the second, third, and fourth columns), it can be observed that the left side of the image exhibits a blueshift, while the right side exhibits a redshift, which is consistent with the results in Figure 7.

For Eq.(34), when $n = 1$, light rays pass through the equatorial plane of the boson star once, and the resulting image is referred to as the direct image. In this case, the light emitted from the accreting material reaches the observer directly, without being significantly influenced by the gravitational field of the boson star. The direct image contributes more than 95% of the total intensity. Therefore, our discussion of redshift images is limited to the direct image. The redshift factor distribution corresponding to the direct image is shown in Figure 7. We fix the angle of field of view at $\beta_{\text{fov}} = 10^\circ$, the coupling parameter at $\alpha = 0.9$, and the observer distance at $r_{\text{bos}} = 200$, keeping the parameter choices consistent with Figure 6. In the images, red and blue pixels correspond to redshift and blueshift, respectively, with deeper colors representing stronger redshift or blueshift, following a linear relationship. It can be observed from the images that when the observer inclination approaches $\theta \rightarrow 0^\circ$ (the first column), only redshift is present, with no blueshift, and the redshift exhibits a symmetric distribution. The initial scalar field ψ_0 does not significantly affect the degree of redshift. When $\theta = 30^\circ$ (the second column), a slight blueshift appears on the left side of the image, causing the overall redshift to shift towards the right. When θ is larger (the third and fourth columns), a distinct blueshift appears on the left side of the image, with a sharp protrusion at the right endpoint of the blueshift region. As θ increases, the blueshift region becomes more concentrated. By comparing the images in each column, it can be seen that when θ is small, gravitational redshift dominates; however, as θ increases, the radial velocity component of the accreting material grows, leading to an increasing contribution from Doppler effect.

5.2 Weakly coupling potential

In this subsection, we fix the initial scalar field at $\psi_0 = 0.08$ and investigate the effect of weak coupling, i.e., a larger coupling parameter α , on the optical images of boson stars. Similar to the previous analysis, we sequentially solve for the numerical solutions of the scalar field ψ and the metric components $-g_{tt}$ and g_{rr} , fit the functions, and generate the optical and redshift images of the boson star.

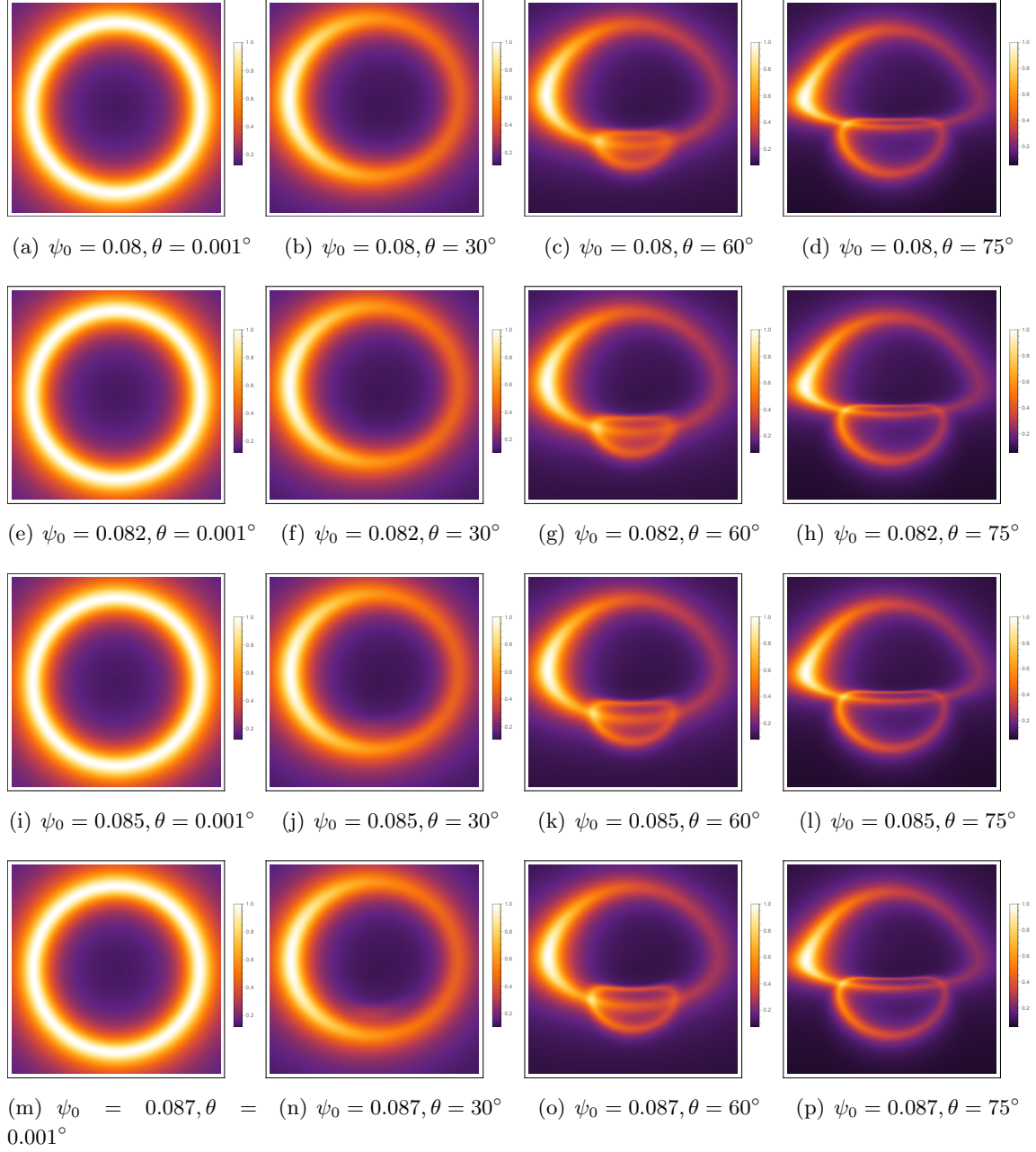


Figure 6: Optical images of boson stars illuminated by a thin accretion disk for different initial scalar field values ψ_0 , with the angle of field of view $\beta_{\text{fov}} = 10^\circ$, the coupling parameter $\alpha = 0.9$, and the observer at $r_{\text{obs}} = 200$. Each row from top to bottom corresponds to $\psi_0 = 0.08, 0.082, 0.085, 0.087$, while each column from left to right corresponds to observer inclination angles $\theta = 0.001^\circ, 30^\circ, 60^\circ, 75^\circ$.

The numerical results of ψ for different values of α are shown in Figure 8. It can be observed that even as α increases from 0.16 to 0.7, ψ exhibits only slight variations and rapidly decays to zero as $r \rightarrow \infty$. The numerical results of the metric components $-g_{tt}$ and g_{rr} are presented in Figure 9, where

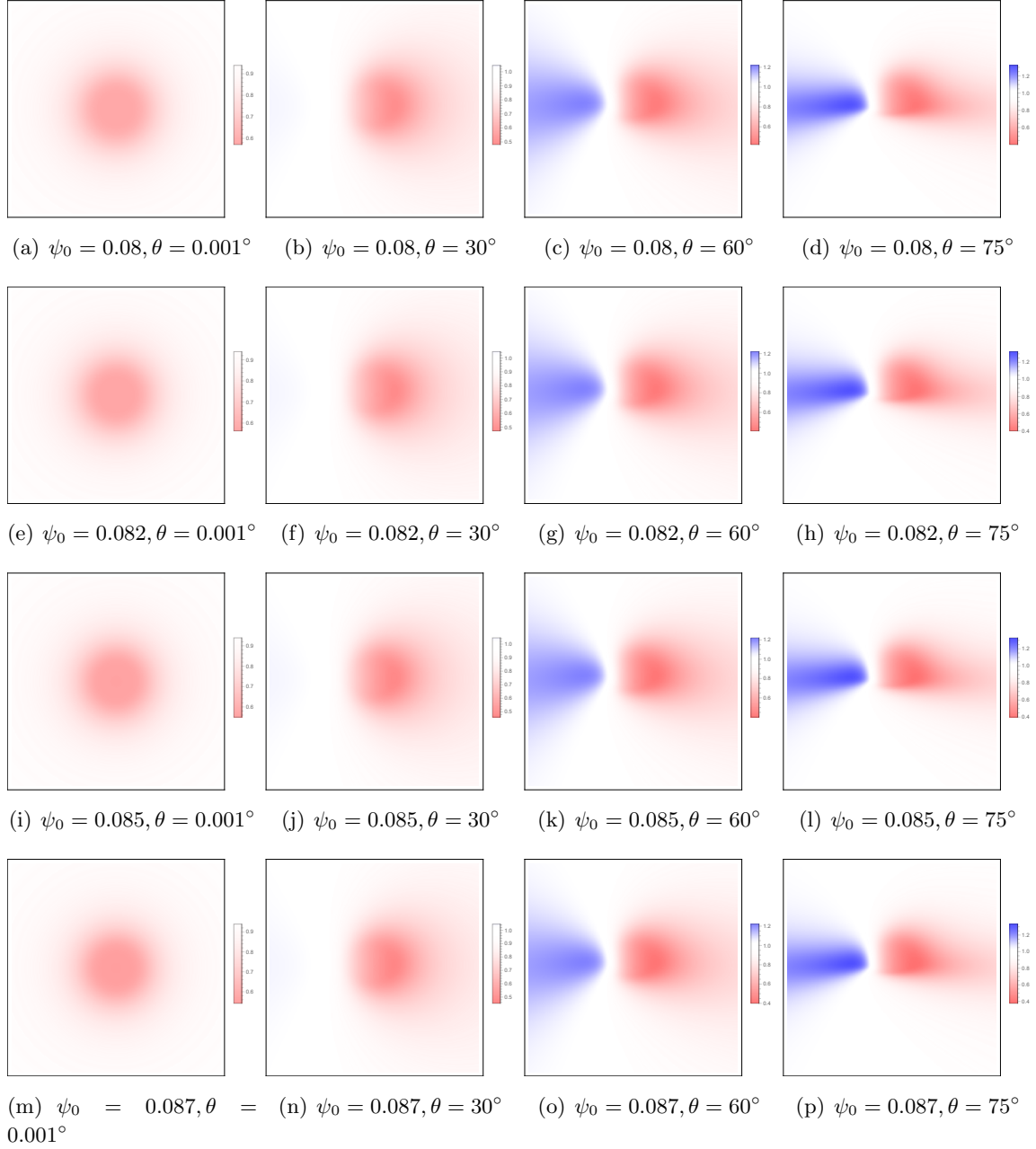


Figure 7: Redshift factor distribution corresponding to the direct image under different initial scalar field ψ_0 , with the coupling parameter $\alpha = 0.9$ and the angle of field of view $\beta_{\text{fov}} = 10^\circ$. Red and blue colors represent redshift and blueshift, respectively, with deeper colors indicating stronger effects, following a linear relationship. Each row from top to bottom corresponds to $\psi_0 = 0.08, 0.082, 0.085, 0.087$, while each column from left to right corresponds to observer inclination angles $\theta = 0.001^\circ, 30^\circ, 60^\circ, 75^\circ$.

the Schwarzschild metric components are plotted as black solid lines for comparison. For a fixed r , as α increases, $-g_{tt}$ decreases while g_{rr} increases. Unlike the Schwarzschild metric components, the metric

components of the boson star do not diverge as $r \rightarrow 0$, whereas the Schwarzschild metric components tend to infinity. This distinction reflects the presence of an event horizon in the Schwarzschild black hole, whereas the boson star lacks an event horizon. On the other hand, as $r \rightarrow \infty$, all metric components asymptotically approach unity, indicating that the spacetime of the boson star is asymptotically flat, similar to the Schwarzschild spacetime.

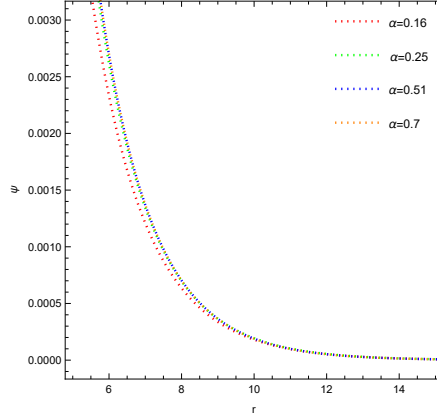


Figure 8: Variation of the scalar field ψ as a function of the radial distance r under weak coupling, with the initial scalar field $\psi_0 = 0.08$.

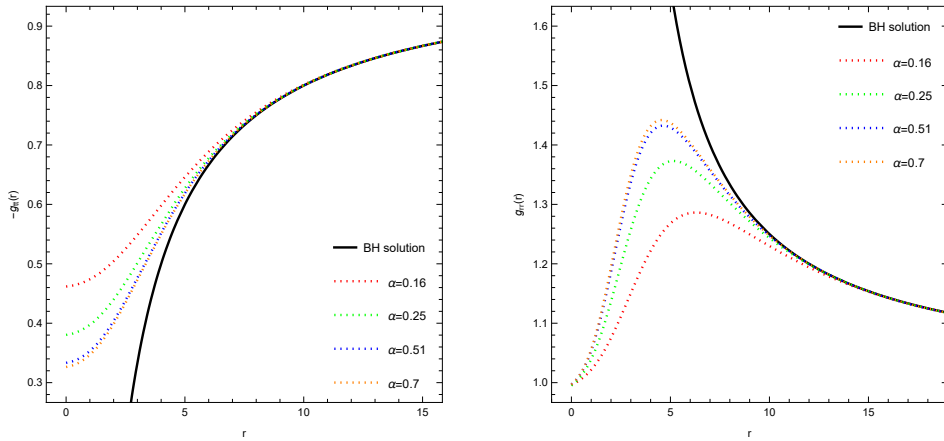


Figure 9: Comparison between the numerical metrics and the Schwarzschild black hole metric components under weak coupling, with the initial scalar field $\psi_0 = 0.08$. The mass of the Schwarzschild BH is 1.

After obtaining the numerical solutions for the metric components, in principle, the optical images of boson stars can be studied using numerical methods. However, due to the presence of numerical infinity, direct calculations using the numerical metric are not feasible. Therefore, we fit the numerical metric using Eq.(39) and (40). The fitting results are shown in Figure 10, where the dashed lines represent the numerical metric components, and the solid lines represent the fitting functions. It can be observed that for different values of α , the two curves almost overlap. As $r \rightarrow \infty$, the fitting

functions asymptotically approach unity, satisfying the requirement of asymptotic flatness. Therefore, the fitting functions can replace the numerical metric components for subsequent calculations. The parameter estimates of the fitting functions are presented in Tables 3 and 4. Additionally, the coupling parameter α is found to be inversely related to the boson star mass $m(r)$.

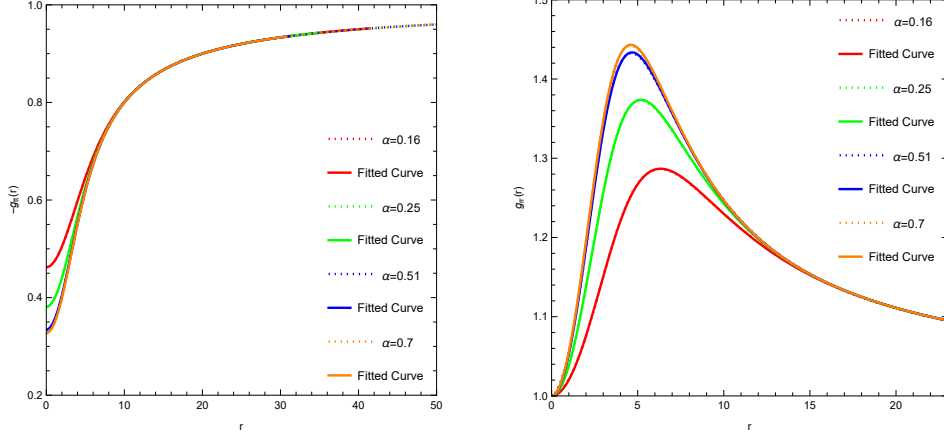


Figure 10: Comparison between the numerical metrics and the fitting functions under weak coupling, with the initial scalar field $\psi_0 = 0.08$. The dashed lines represent the numerical metrics, while the solid lines represent the fitting functions.

Table 3. Parameter estimates of $p_i (i = 1, \dots, 7)$ in the fitting function (39) for the metric component g_{tt} under weak coupling, with the initial scalar field $\psi_0 = 0.08$. $m(r)$ represents the mass of the boson star.

Type	α	$m(r)$	p_1	p_2	p_3	p_4	p_5	p_6	p_7
SBS1	0.16	0.433	0.106	0.124	-0.381	-0.043	-0.063	-0.009	-0.061
SBS2	0.25	0.534	0.056	0.114	-0.373	-0.025	-0.054	-0.008	-0.071
SBS3	0.51	0.591	0.03	0.113	-0.368	-0.015	-0.052	-0.007	-0.078
SBS4	0.7	0.599	0.026	0.113	-0.368	-0.014	-0.051	-0.007	-0.079

Table 4. Parameter estimates of $q_i (i = 1, \dots, 7)$ in the fitting function (40) for the metric component g_{rr} under weak coupling, with the initial scalar field $\psi_0 = 0.08$. $m(r)$ represents the mass of the boson star.

Type	α	$m(r)$	q_1	q_2	q_3	q_4	q_5	q_6	q_7
SBS1	0.16	0.433	-10.343	-1.522	4.217	0.604	1.028	0.026	0.017
SBS2	0.25	0.534	-10.251	-1.35	4.407	0.546	0.999	0.025	0.023
SBS3	0.51	0.591	-17.42	-2.308	6.593	1.043	1.531	0.031	0.019
SBS4	0.7	0.599	-15.783	-2.075	6.122	0.908	1.414	0.03	0.021

We also plot the effective potential of the boson star based on Eq.(26), as shown in Figure 11. In the figure, the dashed lines represent the effective potential of the boson star, while the black solid lines represent the effective potential of the Schwarzschild black hole. It can be observed that the effective potential function of the boson star exhibits a minimum, and as α increases, the minimum

point shifts downward and to the left. In contrast, the effective potential of the Schwarzschild black hole does not have a minimum. As $r \rightarrow \infty$, the effective potentials of both the boson star and the Schwarzschild black hole asymptotically approach zero. This analysis indicates that photon rings exist for the Schwarzschild black hole shadow; however, no photon ring is present in the optical image of the boson star.

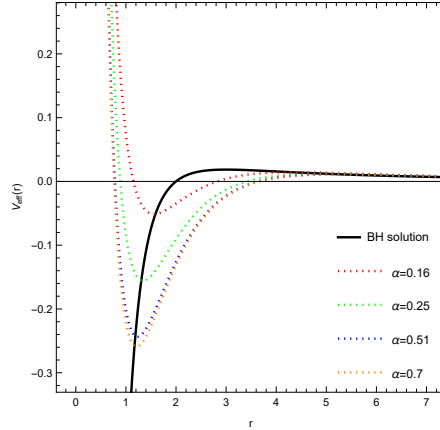


Figure 11: Variation of the effective potential $V_{eff}(r)$ as a function of the radial distance r for boson stars and the Schwarzschild black hole under weak coupling, with the impact parameter $b = 1$ and the initial scalar field $\psi_0 = 0.08$. The dashed lines represent boson stars, while the solid lines represent the Schwarzschild black hole.

The optical images corresponding to different boson stars under a spherical light source are shown in Figure 12. The celestial sphere is divided into four quadrants, where the black transparent region at the center represents the boson star, the outer white circle corresponds to the Einstein ring, and the brown dashed lines inside the Einstein ring indicate photon trajectories. We fix the initial scalar field at $\psi_0 = 0.08$, the observer inclination at $\beta_{fov} = 45^\circ$, and the observer distance at $r_{obs} = 50m(r)$, where $m(r)$ represents the boson star mass. It can be observed from the images that the boson star lacks an event horizon, and the light within the Einstein ring is not completely absorbed. Since the boson star is non-rotating, the black transparent central region appears as a perfect circle, resembling a static black hole, and the background celestial sphere does not exhibit a frame-dragging effect. As α increases, the boson star radius expands, and the photon trajectories within the Einstein ring are altered due to changes in the spacetime geometry.

In realistic scenarios, an accretion disk is expected to exist around the boson star, making the study of optical images illuminated by an accretion disk particularly significant. For simplicity, we assume that the accretion disk is both optically and geometrically thin, located in the equatorial plane, with the observer positioned at $r_{obs} = 200$ and the initial scalar field set to $\psi_0 = 0.08$. The optical images of different boson stars under a thin accretion disk are shown in Figure 13. When $\theta \rightarrow 0$ (the first column), the optical image of the boson star consists only of the direct image, which appears as a symmetric circular ring due to gravitational redshift. When $\theta = 30^\circ$ (the second column), the direct image slightly deforms into an elliptical shape, and the enhanced Doppler effect causes the left side of the direct image to be brighter than the right. As α increases, the shape of the direct image

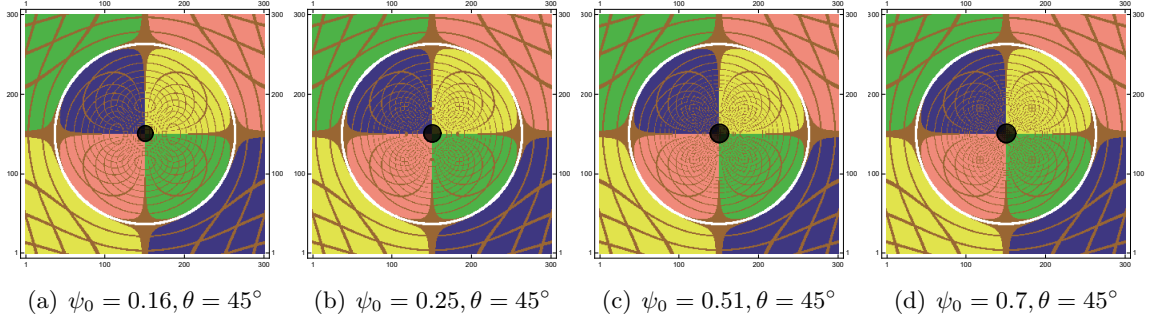


Figure 12: Optical images of boson stars illuminated by a spherical light source under weak coupling, with the initial scalar field $\psi_0 = 0.08$, the angle of field of view $\beta_{\text{fov}} = 45^\circ$, and the observer at $r_{\text{obs}} = 50m(r)$, where $m(r)$ represents the mass of the boson star. The black transparent region represents the boson star, while the white ring corresponds to the Einstein ring.

remains nearly unchanged, but its size increases significantly. When $\theta = 60^\circ$ (the third column), the deformation of the direct image becomes more pronounced. Notably, for smaller values of α (e.g., $\alpha = 0.16$), only the direct image is observed, whereas for larger values of α (e.g., $\alpha = 0.51, 0.7$), a lensed image begins to appear. When $\theta = 75^\circ$ (the fourth column), the direct image deforms into a D-shaped structure, and for larger values of α (e.g., $\alpha = 0.51, 0.7$), the lensed image becomes highly pronounced. This analysis indicates that the coupling parameter α primarily affects the size of the direct image, while the observer inclination θ mainly influences its shape. Larger values of α and θ lead to the emergence of the lensed image, while the Doppler effect results in an asymmetric brightness distribution.

The redshift factor distribution corresponding to the direct image under weak coupling is shown in Figure 14. We fix the observer distance at $r_{\text{obs}} = 200$ and the initial scalar field at $\psi_0 = 0.08$. By comparing the images in each column, it can be observed that the observer inclination θ significantly influences the distribution of the redshift factor. When $\theta \rightarrow 0^\circ$ (the first column), only redshift is present, with no blueshift, and the redshift exhibits a symmetric distribution. As θ increases, the increasing radial velocity component of the accreting material enhances the blueshift factor, while both the blueshift and redshift distributions become more concentrated. By comparing the images in each row, it can be seen that an increase in α does not affect the distribution of redshift and blueshift but enhances the magnitude of the redshift, with the relationship appearing to be linear.

5.3 Strongly coupled potential

In this subsection, we fix the initial scalar field at $\psi_0 = 0.088$ and investigate the effect of strong coupling, i.e., a smaller coupling parameter α , on the optical images of boson stars. Similar to the previous analysis, for different values of α , the scalar field ψ rapidly decays and asymptotically approaches zero. We also compute the numerical solutions of the metric components $-g_{tt}$ and g_{rr} and fit them using Eqs.(39) and (40), ensuring that the fitting functions satisfy the asymptotic flatness condition. The parameter estimates are presented in Tables 5 and 6. These results reveal that as α

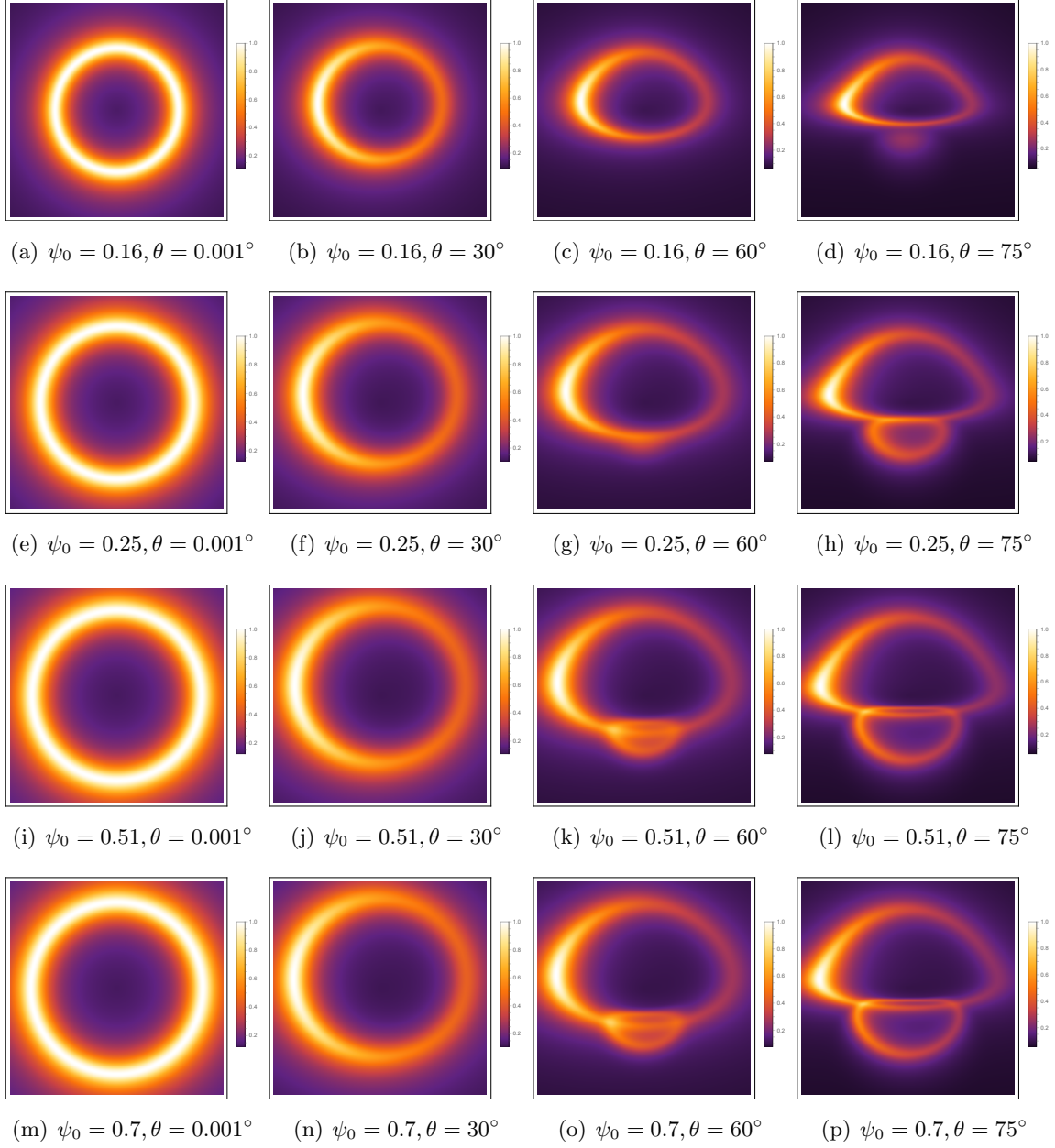


Figure 13: Optical images of boson stars illuminated by a thin accretion disk under weak coupling, with the angle of field of view $\beta_{\text{fov}} = 3^\circ$, the initial scalar field $\psi_0 = 0.08$, and the observer at $r_{\text{obs}} = 200$. Each row from top to bottom corresponds to coupling parameters $\alpha = 0.16, 0.25, 0.51, 0.7$, while each column from left to right corresponds to observer inclination angles $\theta = 0.001^\circ, 30^\circ, 60^\circ, 75^\circ$.

increases, the boson star mass $m(r)$ exhibits a decreasing trend. In subsequent calculations, the fitting functions are used in place of the numerical metric.

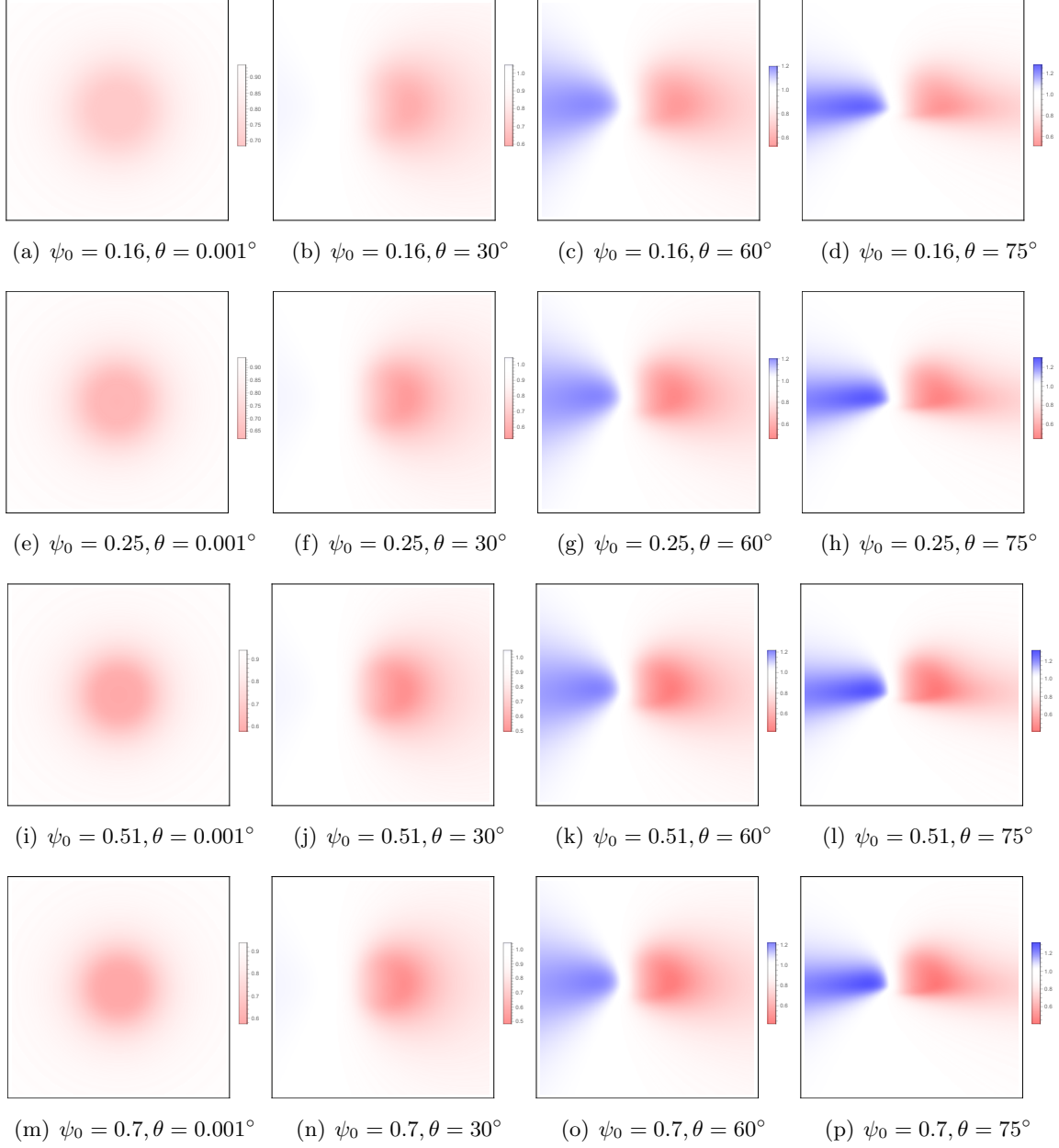


Figure 14: Redshift factor distribution corresponding to the direct image under weak coupling, with the initial scalar field $\psi_0 = 0.08$ and the angle of field of view $\beta_{\text{fov}} = 10^\circ$. Red and blue colors represent redshift and blueshift, respectively, with deeper colors indicating stronger effects, following a linear relationship. Each row from top to bottom corresponds to coupling parameters $\alpha = 0.16, 0.25, 0.51, 0.7$, while each column from left to right corresponds to observer inclination angles $\theta = 0.001^\circ, 30^\circ, 60^\circ, 75^\circ$.

Table 5. Parameter estimates of $p_i (i = 1, \dots, 7)$ in the fitting function (39) for the metric component g_{tt} under strong coupling, with $\psi_0 = 0.088$. $m(r)$ represents the mass of the boson star.

Type	α	$m(r)$	p_1	p_2	p_3	p_4	p_5	p_6	p_7
SBS1	0.077	1.263	-0.254	0.05	-0.271	0.063	-0.011	-0.001	-0.059
SBS2	0.076	1.329	-0.251	0.048	-0.266	0.061	-0.01	-0.001	-0.061
SBS3	0.075	1.371	-0.25	0.048	-0.268	0.06	-0.01	-0.001	-0.067
SBS4	0.0733	1.41	-0.246	0.046	-0.26	0.057	-0.01	-0.001	-0.066

Table 6. Parameter estimates of $q_i (i = 1, \dots, 7)$ in the fitting function (40) for the metric component g_{rr} under strong coupling, with ψ_0 0.088. $m(r)$ represents the mass of the boson star.

Type	α	$m(r)$	q_1	q_2	q_3	q_4	q_5	q_6	q_7
SBS1	0.077	1.263	-6.732	-1.05	213.839	-27.778	-3.462	1.699	1.844
SBS2	0.076	1.329	-4.516	-1.298	113.743	25.694	-14.011	2.474	2.169
SBS3	0.075	1.371	-4.518	-0.989	77.762	12.166	-7.204	1.433	1.732
SBS4	0.0733	1.41	-13.833	-0.429	145.126	-23.899	1.953	0.615	1.054

The optical images of boson stars illuminated by a spherical light source under strong coupling are shown in Figure 15. We fix the initial scalar field at $\psi_0 = 0.088$, the observer inclination at $\beta_{\text{fov}} = 45^\circ$, and the observer distance at $r_{\text{obs}} = 50m(r)$, where $m(r)$ represents the boson star mass. The red, blue, yellow, and green regions correspond to the four quadrants of the celestial sphere, with the boson star located at the center of the sphere. From the images, it can be observed that as α decreases, the size of the boson star increases significantly. Within the Einstein ring, the background celestial sphere does not exhibit a frame-dragging effect. Specifically, the boundary between the blue and yellow quadrants is perpendicular to the horizontal axis, which is a direct consequence of the non-rotating nature of the boson star.

It is worth noting that a sub-annular structure also appears within the Einstein ring. For black hole shadows, the sub-annular structure refers to the ring-like structure within the photon ring, which is caused by gravitational refraction of light. According to [69], if a bubble made of non-emitting matter of zero optical depth exists around a static black hole, this configuration is stable under a physically reasonable set of parameters and can generate observable distortions in the rings pattern of the image [70], which correspond to gravitationally lensed secondary images created by the photon ring. This phenomenon generates the sub-annular structure within the photon ring and does not depend on exotic matter or strange spacetime contortions. In the optical images of the boson star under strong coupling, sub-annular structures similar to those in black hole shadows also appear. It can be observed that as α decreases, the number of sub-annular increases.

The optical images of boson stars illuminated by a thin accretion disk under strong coupling are shown in Figure 16. The observer is positioned at $r_{\text{obs}} = 200$, and the initial scalar field is set to $\psi_0 = 0.088$. When the observer inclination approaches $\theta \rightarrow 0^\circ$ (the first column), the outermost bright ring in the optical image corresponds to the direct image. As α decreases, the size of the direct image gradually increases, but its shape remains a symmetric circular ring. Notably, in addition to the direct image ($n = 1$), multiple lensed images ($n = 2$) appear in the optical images. These lensed images are formed by photons that orbit the equatorial plane of the boson star twice. They exhibit multiple concentric rings distributed inside the direct image. Within the innermost lensed image, a central brightness depression emerges, resembling the inner shadow of a black hole [63]. This

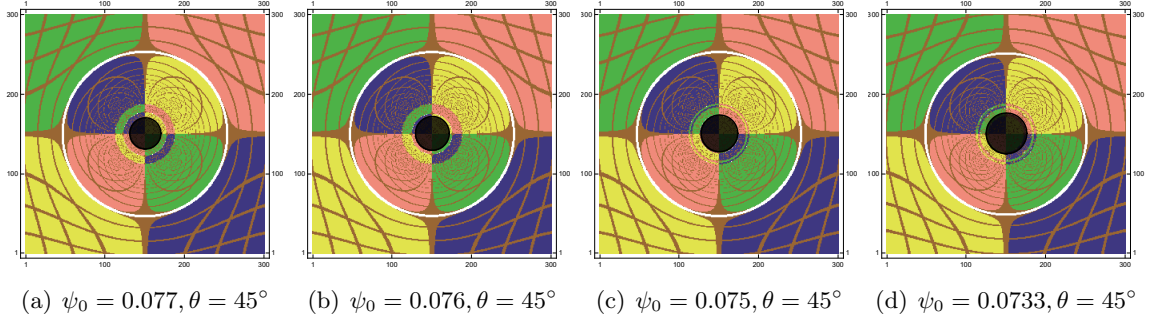


Figure 15: Optical images of boson stars illuminated by a spherical light source under strong coupling, with the initial scalar field $\psi_0 = 0.088$, the angle of field of view $\beta_{\text{fov}} = 45^\circ$, and the observer at $r_{\text{obs}} = 50m(r)$, where $m(r)$ represents the mass of the boson star. The black transparent region represents the boson star, while the white ring corresponds to the Einstein ring.

phenomenon suggests that under specific parameter choices, the optical images of boson stars and black hole shadows may be difficult to distinguish. When $\theta = 17^\circ$ (the second column), the direct and lensed images slightly shift downward on the screen. As θ increases to 45° and 70° (the third and fourth columns), the direct and lensed images begin to overlap. Particularly, when $\theta = 70^\circ$ (the fourth column), the lensed images shift significantly downward, while the direct image deforms into a D-shaped structure. A hat-shaped dark region appears at the center of the image, closely resembling the inner shadow of a black hole. As α decreases, the sizes of both the direct and lensed images increase, whereas the size of the hat-shaped dark region decreases. By comparing each row, it can also be observed that as α decreases, the number of lensed images increases significantly.

Under strong coupling, the redshift factor distribution corresponding to the direct image is shown in Figure 17. Similar to the weak coupling case, an increase in θ significantly affects the distribution of the redshift factor and enhances the degree of blueshift, while a decrease in α slightly enhances the redshift. However, unlike the weak coupling case (see Figure 14), the redshift factor distribution in the strong coupling regime is more concentrated at the center of the image, forming a disk-like region when $\theta \rightarrow 0^\circ$ (the first column) or a hat-shaped region when $\theta = 70^\circ$ (the fourth column). This corresponds to the central brightness depression observed in Figure 16. Compared to the redshift factor near the inner shadow of a black hole, the redshift factor in a boson star appears within the star itself, as the boson star lacks an event horizon.

6 Conclusions and discussions

This paper investigates the optical properties of solitonic boson stars. Using the backward ray-tracing techniques, we analyze the effects of the initial scalar field ψ_0 , the coupling parameter α , and the observer inclination angle θ on the photon trajectories and optical images of solitonic boson stars. Two types of light sources are considered: spherical light sources and thin accretion disks located in the equatorial plane. Additionally, we numerically compute the effective potential and redshift factor. The results reveal both the similarities and key differences between the optical images of solitonic

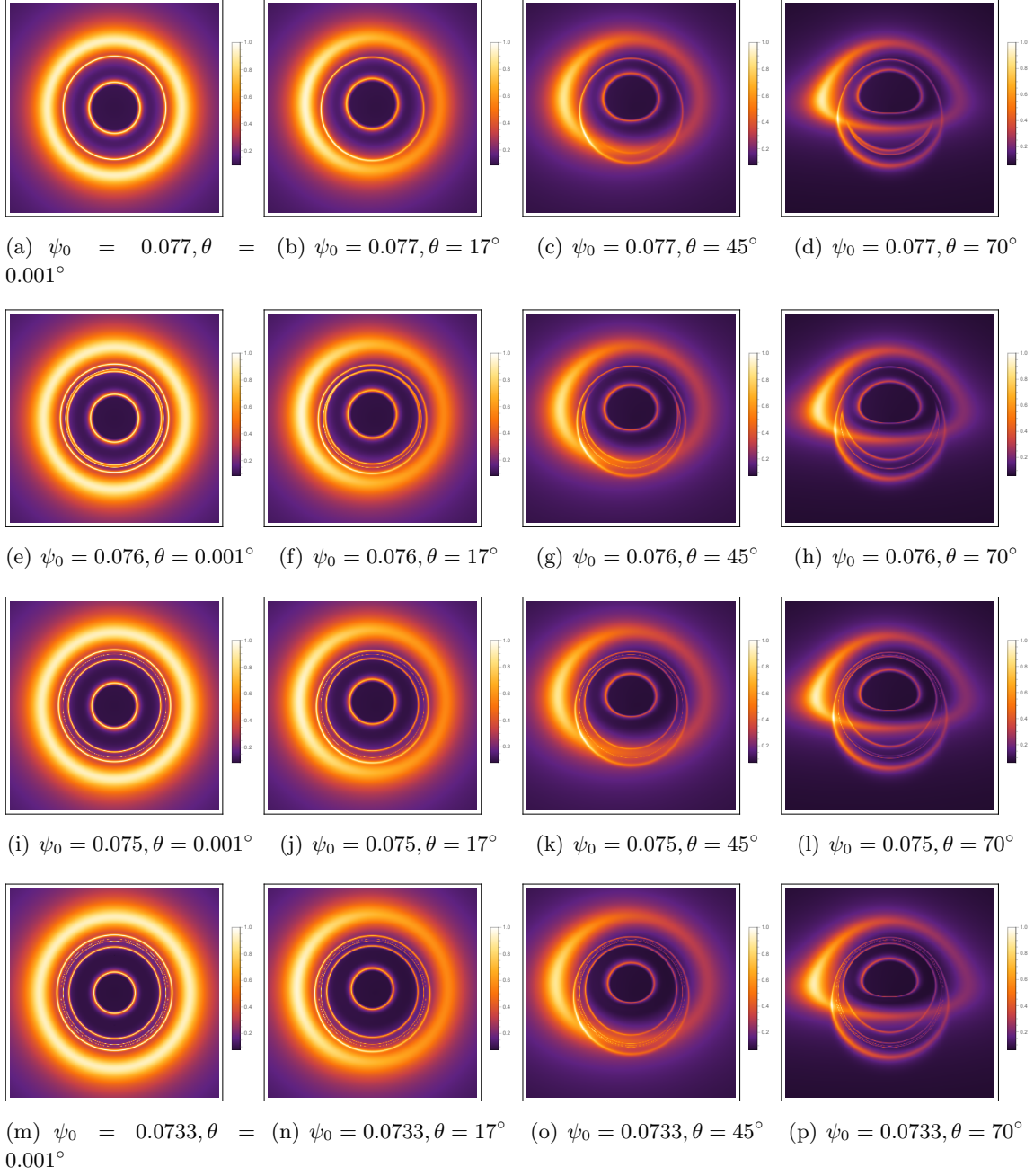


Figure 16: Optical images of boson stars illuminated by a thin accretion disk under strong coupling, with the angle of field of view $\beta_{\text{fov}} = 8^\circ$, the initial scalar field $\psi_0 = 0.088$, and the observer at $r_{\text{obs}} = 200$. Each row from top to bottom corresponds to coupling parameters $\alpha = 0.077, 0.076, 0.075, 0.0733$, while each column from left to right corresponds to observer inclination angles $\theta = 0.001^\circ, 17^\circ, 45^\circ, 70^\circ$.

boson stars and black hole shadows, providing theoretical support for distinguishing solitonic boson stars from black holes in future high-resolution astronomical observations.

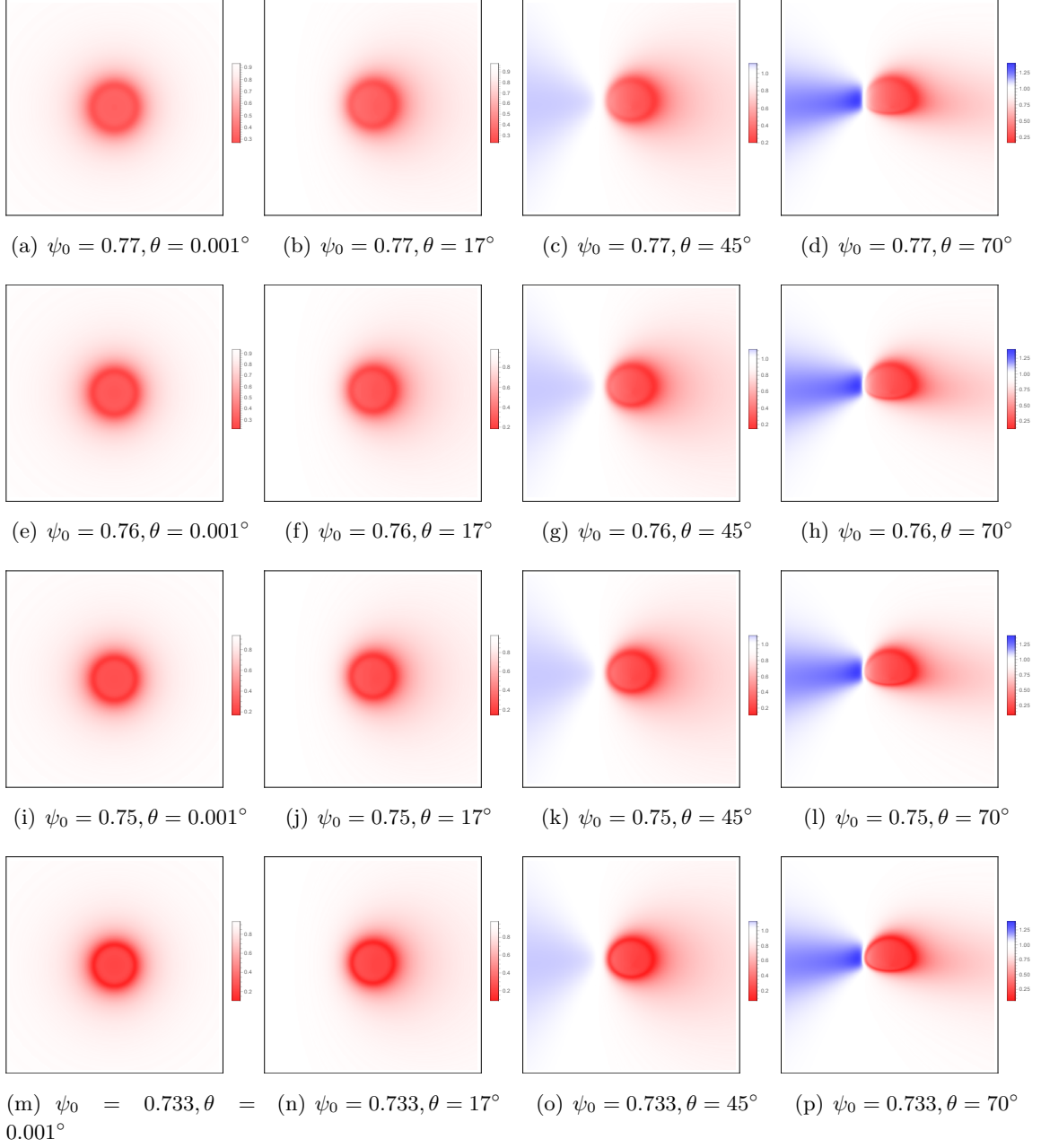


Figure 17: Redshift factor distribution corresponding to the direct image under strong coupling, with the initial scalar field $\psi_0 = 0.088$ and the angle of field of view $\beta_{\text{fov}} = 10^\circ$. Red and blue colors represent redshift and blueshift, respectively, with deeper colors indicating stronger effects, following a linear relationship. Each row from top to bottom corresponds to coupling parameters $\alpha = 0.077, 0.076, 0.075, 0.0733$, while each column from left to right corresponds to observer inclination angles $\theta = 0.001^\circ, 17^\circ, 45^\circ, 70^\circ$.

We first examine the effects of the initial scalar field ψ_0 and a larger coupling parameter α (weak

coupling). The non-rotating nature of boson stars implies the absence of the frame-dragging effect under a spherical light source, resembling a static black hole. The influence of ψ_0 on the optical images of boson stars under spherical light sources is insignificant, whereas variations in α significantly alter photon trajectories inside the Einstein ring. In the optical images under a thin accretion disk, the direct image dominates, with ψ_0 and α primarily affecting the size of the optical image, while the observer inclination angle θ predominantly influences its shape. When θ is small, the optical image appears as a single bright ring with a central brightness depression, which is similar to the observations of the EHT, where gravitational redshift dominates. As θ increases, the Doppler effect becomes more pronounced, leading to a significant brightness contrast between the left and right sides of the direct image. Moreover, for larger θ , a lensed image emerges, with larger ψ_0 and α leading to an increase in its size. In this scenario, the distribution of the redshift factor is sensitive to θ , while the intensity of the optical image primarily depends on α .

Subsequently, we consider the effects of a smaller coupling parameter α (strong coupling). In contrast to the previous cases, a smaller value of α leads to the formation of a sub-annular structure within the Einstein ring, while the size of the boson star is inversely proportional to α . It is worth noting that in the optical images under a thin accretion disk, in addition to the direct images, a smaller α gives rise to lensed images. Among these, the innermost lensed image exhibits significantly lower intensity compared to other regions, resembling the inner shadow of a black hole. This suggests that, for certain parameter choices, the optical images of boson stars may become indistinguishable from black hole shadows. As α decreases, the number of lensed images increases, indicating that light deflection becomes stronger. Meanwhile, an increase in θ leads to significant distortions of both the direct and lensed images. Since boson stars lack an event horizon, under strong coupling, the redshift factor corresponding to the direct image is concentrated within the boson star itself, and an increase in θ enhances the blue shift effect.

Our results emphasize the crucial role of high-resolution observations in distinguishing solitonic boson stars from black holes. The variations in the optical images of boson stars under different parameters and the distribution of their redshift factors provide new possibilities for detecting compact objects. Future research will further consider more realistic accretion disk models, such as thick accretion disks, and modified gravity theories, such as $f(R)$ gravity. These studies will deepen our understanding of compact objects and contribute to distinguishing boson stars from black holes.

Acknowledgments

This work is supported by the National Natural Science Foundation of China (Grant Nos. 11875095 and 11903025) and by the Natural Science Foundation of Chongqing (CSTB2023NSCQ-MSX0594).

References

- [1] L. C. Crispino and D. J. Kennefick, *Nature Physics* **15**, 5 (2019).
- [2] F. W. Dyson, A. S. Eddington and C. Davidson, *Philosophical Transactions of the Royal Society of London. Series A, Containing Papers of a Mathematical or Physical Character* **220**, 291 (1920).
- [3] K. Akiyama *et al.* [Event Horizon Telescope], *Astrophys. J. Lett.* **875**, L1 (2019).

- [4] J. Wambsganss, Living Reviews in Relativity **1**, pp1-74 (2019).
- [5] J. P. Luminet, Astron. Astrophys. **75**, 228-235 (1979).
- [6] H. Falcke, F. Melia and E. Agol, Astrophys. J. Lett. **528**, L13 (2000).
- [7] K. Akiyama *et al.* [Event Horizon Telescope], Astrophys. J. Lett. **930**, no.2, L12 (2022).
- [8] D. Psaltis *et al.* [Event Horizon Telescope], Phys. Rev. Lett. **125**, no.14, 141104 (2020).
- [9] Y. Hou, P. Liu, M. Guo, H. Yan and B. Chen, Class. Quant. Grav. **39**, no.19, 194001 (2022).
- [10] P. V. P. Cunha and C. A. R. Herdeiro, Gen. Rel. Grav. **50**, no.4, 42 (2018).
- [11] C. Cunningham and J. M. Bardeen, Astrophys. J. Lett. **173**, L137 (1972).
- [12] V. Cardoso and R. Vicente, Phys. Rev. D **100**, no.8, 084001 (2019).
- [13] V. Cardoso, F. Duque and A. Foschi, Phys. Rev. D **103**, no.10, 104044 (2021).
- [14] F. H. Vincent, S. E. Gralla, A. Lupsasca and M. Wielgus, Astron. Astrophys. **667**, A170 (2022).
- [15] G. Lara, S. H. Völkel and E. Barausse, Phys. Rev. D **104**, no.12, 124041 (2021).
- [16] M. Wielgus, Phys. Rev. D **104**, no.12, 124058 (2021).
- [17] F. H. Vincent, M. Wielgus, M. A. Abramowicz, E. Gourgoulhon, J. P. Lasota, T. Paumard and G. Perrin, Astron. Astrophys. **646**, A37 (2021).
- [18] R. Narayan, M. D. Johnson and C. F. Gammie, Astrophys. J. Lett. **885**, no.2, L33 (2019).
- [19] X. X. Zeng, H. Q. Zhang and H. Zhang, Eur. Phys. J. C **80**, no.9, 872 (2020).
- [20] M. Heydari-Fard, M. Heydari-Fard and N. Riazi, Int. J. Mod. Phys. D **32**, no.13, 2350088 (2023).
- [21] S. E. Gralla, D. E. Holz and R. M. Wald, Phys. Rev. D **100**, no. 2, 024018 (2019).
- [22] X. X. Zeng and H. Q. Zhang, Eur. Phys. J. C **80**, no.11, 1058 (2020).
- [23] J. Peng, M. Guo and X. H. Feng, Chin. Phys. C **45**, no.8, 085103 (2021).
- [24] K. J. He, S. C. Tan and G. P. Li, Eur. Phys. J. C **82**, no.1, 81 (2022).
- [25] G. P. Li and K. J. He, Eur. Phys. J. C **81**, no.11, 1018 (2021).
- [26] X. X. Zeng, K. J. He and G. P. Li, Sci. China Phys. Mech. Astron. **65**, no.9, 290411 (2022).
- [27] S. Guo, K. J. He, G. R. Li and G. P. Li, Class. Quant. Grav. **38**, no.16, 165013 (2021).
- [28] G. P. Li and K. J. He, JCAP **06**, 037 (2021).
- [29] X. J. Gao, T. T. Sui, X. X. Zeng, Y. S. An and Y. P. Hu, Eur. Phys. J. C **83**, 1052 (2023).
- [30] Y. H. Cui, S. Guo, Y. X. Huang, Y. Liang and K. Lin, Eur. Phys. J. C **84**, no.8, 772 (2024).
- [31] K. J. He, S. Guo, S. C. Tan and G. P. Li, Chin. Phys. C **46**, no.8, 085106 (2022).
- [32] H. M. Wang, Z. C. Lin and S. W. Wei, Nucl. Phys. B **985**, 116026 (2022).
- [33] Y. Hou, Z. Zhang, H. Yan, M. Guo and B. Chen, Phys. Rev. D **106**, no.6, 064058 (2022).
- [34] C. Y. Yang, M. I. Aslam, X. X. Zeng and R. Saleem, JHEAp **46**, 345 (2025).
- [35] S. Guo, Y. X. Huang, E. W. Liang, Y. Liang, Q. Q. Jiang and K. Lin, Astrophys. J. **975**, no.2, 237 (2024).

- [36] K. J. He, G. P. Li, C. Y. Yang and X. X. Zeng, arXiv:2411.11680 [astro-ph.HE].
- [37] G. P. Li, H. B. Zheng, K. J. He and Q. Q. Jiang, arXiv:2410.17295 [gr-qc].
- [38] K. J. He, J. T. Yao, X. Zhang and X. Li, Phys. Rev. D **109**, no.6, 064049 (2024).
- [39] X. X. Zeng, L. F. Li, P. Li, B. Liang and P. Xu, Sci. China Phys. Mech. Astron. **68**, no.2, 220412 (2025).
- [40] X. X. Zeng, K. J. He, J. Pu, G. p. Li and Q. Q. Jiang, Eur. Phys. J. C **83**, no.10, 897 (2023).
- [41] Y. Liu, Q. Chen, X. X. Zeng, H. Zhang, W. L. Zhang and W. Zhang, JHEP **10**, 189 (2022).
- [42] K. J. He, Y. W. Han and G. P. Li, Nucl. Phys. B **1010**, 116768 (2025).
- [43] G. P. Li, K. J. He, X. Y. Hu and Q. Q. Jiang, Front. Phys. (Beijing) **19**, no.5, 54202 (2024).
- [44] K. J. He, Y. W. Han and G. P. Li, Phys. Dark Univ. **44**, 101468 (2024).
- [45] V. Cardoso and P. Pani, Living Rev. Rel. **22**, no.1, 4 (2019).
- [46] L. Barack, V. Cardoso, S. Nissanke, T. P. Sotiriou, A. Askar, C. Belczynski, G. Bertone, E. Bon, D. Blas and R. Brito, *et al.* Class. Quant. Grav. **36**, no.14, 143001 (2019).
- [47] M. Wielgus, J. Horak, F. Vincent and M. Abramowicz, Phys. Rev. D **102**, no.8, 084044 (2020).
- [48] N. Tsukamoto, Phys. Rev. D **104**, no.6, 064022 (2021).
- [49] G. J. Olmo, D. Rubiera-Garcia and D. S. C. Gómez, Phys. Lett. B **829**, 137045 (2022).
- [50] M. Guerrero, G. J. Olmo, D. Rubiera-Garcia and D. Gómez Sáez-Chillón, Phys. Rev. D **105**, no.8, 084057 (2022).
- [51] N. Tsukamoto, Phys. Rev. D **105**, no.8, 084036 (2022).
- [52] P. V. P. Cunha, E. Berti and C. A. R. Herdeiro, Phys. Rev. Lett. **119**, no.25, 251102 (2017).
- [53] D. J. Kaup, Phys. Rev. **172**, 1331-1342 (1968).
- [54] R. Ruffini and S. Bonazzola, Phys. Rev. **187**, 1767-1783 (1969).
- [55] S. L. Liebling and C. Palenzuela, Living Rev. Rel. **26**, no.1, 1 (2023).
- [56] F. Di Giovanni, N. Sanchis-Gual, P. Cerdá-Durán, M. Zilhão, C. Herdeiro, J. A. Font and E. Radu, Phys. Rev. D **102**, no.12, 124009 (2020).
- [57] F. H. Vincent, Z. Meliani, P. Grandclement, E. Gourgoulhon and O. Straub, Class. Quant. Grav. **33**, no.10, 105015 (2016).
- [58] A. Masó-Ferrando, N. Sanchis-Gual, J. A. Font and G. J. Olmo, Class. Quant. Grav. **38**, no.19, 194003 (2021).
- [59] J. L. Rosa, C. F. B. Macedo and D. Rubiera-Garcia, Phys. Rev. D **108**, no.4, 044021 (2023).
- [60] J. L. Rosa, J. Pelle and D. Pérez, Phys. Rev. D **110**, no.8, 084068 (2024).
- [61] X. X. Zeng, C. Y. Yang, Y. X. Huang, K. J. He, G. P. Li and S. Guo, arXiv:2501.13764 [gr-qc].
- [62] C. A. R. Herdeiro, A. M. Pombo, E. Radu, P. V. P. Cunha and N. Sanchis-Gual, JCAP **04**, 051 (2021).
- [63] J. L. Rosa and D. Rubiera-Garcia, Phys. Rev. D **106**, no.8, 084004 (2022).

- [64] L. G. Collodel and D. D. Doneva, Phys. Rev. D **106**, no.8, 084057 (2022).
- [65] S. R. Coleman, Nucl. Phys. B **262**, no.2, 263 (1985).
- [66] R. Friedberg, T. D. Lee and A. Sirlin, Phys. Rev. D **13**, 2739-2761 (1976).
- [67] R. N. Cahn, Nucl. Phys. B **255**, 341 (1985).
- [68] G. P. Li, H. B. Zheng, K. J. He and Q. Q. Jiang, arXiv:2410.17295 [gr-qc].
- [69] G. Giribet, E. R. de Celis and P. Schmied, Gen. Rel. Grav. **56**, no.9, 106 (2024).
- [70] A. E. Broderick, D. W. Pesce, P. Tiede, H. Y. Pu, R. Gold, R. Anantua, S. Britzen, C. Ceccobello, K. Chatterjee and Y. Chen, *et al.* Astrophys. J. **935**, 61 (2022).